Widespread collapse of the Ross Ice Shelf during the late Holocene

Yusuke Yokoyama[a,b,c,1], John B. Anderson[d], Masako Yamane[a,c], Lauren M. Simkins[d], Yosuke Miyairi[a], Takahiro Yamazaki[a,b], Mamito Koizumi[a,b], Hisami Suga[c], Kazuya Kusahara[e], Lindsay Prothro[d], Hiroyasu Hasumi[a], John R. Southon[f], and Naohiko Ohkouchi[c]

[a]Atmosphere and Ocean Research Institute, The University of Tokyo, 5-1-5 Kashiwa-no-ha, Kashiwa 275-8564, Japan; [b]Department of Earth and Planetary Science, The University of Tokyo, 7-3-1 Hongo, Bunkyo-ku, Tokyo 113-0033, Japan; [c]Department of Biogeochemistry, Japan Agency for Marine-Earth Science and Technology, 2-15 Natsushima-cho, Yokosuka 237-0061, Japan; [d]Department of Earth Science, Rice University, Houston, TX 77005; [e]Antarctic Climate & Ecosystems Cooperative Research Centre, Hobart, Tasmania 7001, Australia; and [f]Department of Earth System Science, University of California, Irvine, CA 92697

Edited by Mark H. Thiemens, University of California at San Diego, La Jolla, CA, and approved January 15, 2016 (received for review August 25, 2015)

The stability of modern ice shelves is threatened by atmospheric and oceanic warming. The geologic record of formerly glaciated continental shelves provides a window into the past of how ice shelves responded to a warming climate. Fields of deep (−560 m), linear iceberg furrows on the outer, western Ross Sea continental shelf record an early post-Last Glacial Maximum episode of ice-shelf collapse that was followed by continuous retreat of the grounding line for ∼200 km. Runaway grounding line conditions culminated once the ice became pinned on shallow banks in the western Ross Sea. This early episode of ice-shelf collapse is not observed in the eastern Ross Sea, where more episodic grounding line retreat took place. More widespread (∼280,000 km^2) retreat of the ancestral Ross Ice Shelf occurred during the late Holocene. This event is recorded in sediment cores by a shift from terrigenous glacimarine mud to diatomaceous open-marine sediment as well as an increase in radiogenic beryllium (^{10}Be) concentrations. The timing of ice-shelf breakup is constrained by compound specific radiocarbon ages, the first application of this technique systematically applied to Antarctic marine sediments. Breakup initiated around 5 ka, with the ice shelf reaching its current configuration ∼1.5 ka. In the eastern Ross Sea, the ice shelf retreated up to 100 km in about a thousand years. Three-dimensional thermodynamic ice-shelf/ocean modeling results and comparison with ice-core records indicate that ice-shelf breakup resulted from combined atmospheric warming and warm ocean currents impinging onto the continental shelf.

ice shelf | Antarctica | radiocarbon | Ross Sea | ice sheet

Ice shelves are among the most rapidly changing elements of the modern cryosphere, due to their internal weaknesses, atmospheric warming, and melting from beneath by warm ocean currents. In the northern Antarctic Peninsula, accelerated atmospheric warming is the principle cause of ongoing ice-shelf retreat (1, 2), and collapse of the Larsen Ice Shelf has resulted in rapid retreat of tidewater glaciers flowing into the ice shelf (2, 3). Farther south in Pine Island Bay, thermal erosion of the floating terminus of Pine Island Glacier by impinging Circumpolar Deep Water (CDW) results in basal melt rates of 6–12.5 m·y^{-1} and is causing rapid grounding line retreat that poses a threat of ice-stream collapse in the foreseeable future (4, 5). Geological evidence for ice-shelf collapse has been reported for Marguerite Bay in the southern Antarctic Peninsula (6, 7) and in Pine Island Bay in West Antarctica (8, 9), but the timing and rate of these events are poorly constrained.

The modern Ross Ice Shelf is the largest ice shelf on Earth, covering an area of ∼500,000 km^2. It provides a buttress to the outflow of several large outlet glaciers and ice streams that drain the West Antarctic ice sheet (WAIS) and East Antarctic Ice Sheet (EAIS) and thus plays a crucial role in ice-sheet stability (10, 11). Here we report compelling geomorphological, sedimentological, and geochemical evidence for widespread retreat of the Ross Ice Shelf at ∼5 ka to 1.5 ka. Modeling results and comparison with ice-core records indicate that ice-shelf breakup was triggered by oceanic and atmospheric warming.

Results and Discussion

Geological and Geochemical Reconstructions of Past Ice Shelf. During the Last Glacial Maximum (LGM), a much expanded ice sheet extended across the Antarctic continental shelf (12, 13). In the Ross Sea, the LGM ice sheet left its mark on the sea floor in the form of spectacular subglacial geomorphic features, including drumlinoids and megascale glacial lineations and subglacial deposits (till), which have been sampled in many sediment cores across the shelf (14). These combined results demonstrate that the LGM ice sheet was nourished more or less equally by the WAIS and EAIS. Timing of ice sheet retreat since the LGM remains controversial due to limited age constraints (15–22).

Newly acquired (NBP1502A; NBP indicates the research ship *Nathaniel B. Palmer*) high-resolution multibeam swath bathymetry data from the outer continental shelf in the western Ross Sea reveal fields of iceberg furrows that are concentrated in water depths around −560 m (Fig. 1*B*). These features mark an early episode of ice-shelf collapse when the calving line reached the grounding line. Back-stepping grounding line marginal features, including grounding zone wedges and recessional moraines, extend continuously southward for nearly 200 km within the JOIDES Trough and indicate "runaway" grounding line conditions following ice-shelf collapse (Fig. 1*C*). A single radiocarbon age from core NBP 01502A-KC48 in outer JOIDES Trough (Fig. 1*A*) constrains this initial ice-shelf

Significance

The Ross Sea is a major drainage basin for the Antarctic Ice Sheet and contains the world's largest ice shelf. Newly acquired swath bathymetry data and sediment cores provide evidence for two episodes of ice-shelf collapse. Two novel geochemical proxies, compound specific radiocarbon dating and radiogenic beryllium (^{10}Be), constrain the timing of the most recent and widespread (∼280,000 km^2) breakup as having occurred in the late Holocene. Three-dimensional ice-shelf/ocean modeling results and comparison with ice-core records indicate that oceanic and atmospheric warming caused ice-shelf collapse.

Author contributions: Y.Y., J.B.A., and N.O. designed research; Y.Y., M.Y., L.M.S., Y.M., T.Y., M.K., H.S., K.K., L.P., H.H., and J.R.S. performed research; Y.Y. and N.O. contributed new reagents/analytic tools; Y.Y. analyzed data; and Y.Y. and J.B.A. wrote the paper.

The authors declare no conflict of interest.

This article is a PNAS Direct Submission.

Freely available online through the PNAS open access option.

[1]To whom correspondence should be addressed. Email: yokoyama@aori.u-tokyo.ac.jp.

This article contains supporting information online at www.pnas.org/lookup/suppl/doi:10.1073/pnas.1516908113/-/DCSupplemental.

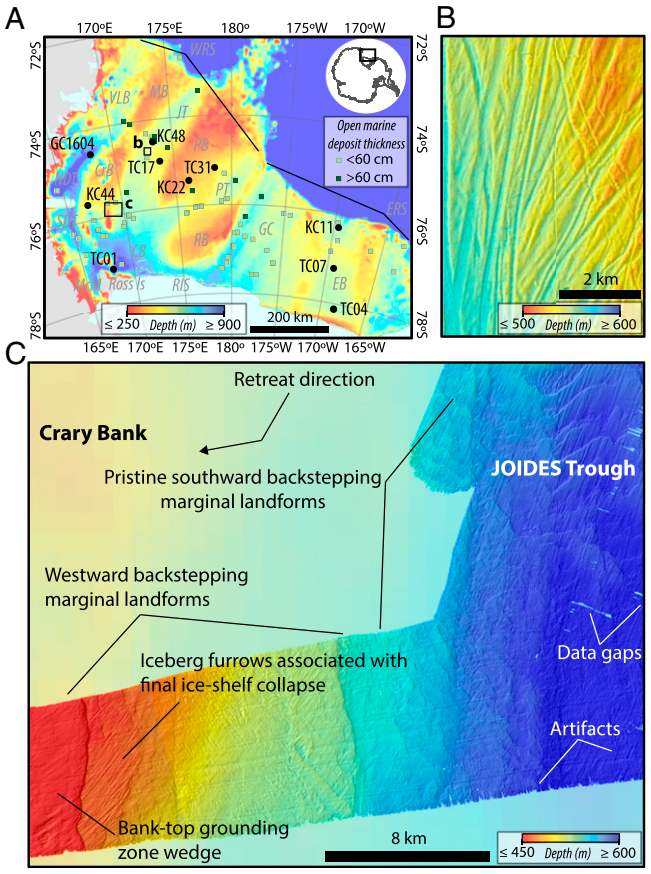

Fig. 1. (*A*) Bathymetric map and location of sediment cores used in this study (black circles), collected on NBP cruises NBP94-01, NBP99- 02, and NBP15-02 and R/V Hakurei Maru cruise TH95. Squares designate cores that sampled diatomaceous muds resting on terrigenous glacimarine mud with colors corresponding to thickness of the diatomaceous muds from cruises NBP94-01, NBP 95-01, and NBP 99-02. (*B*) Multibeam swath bathymetric image of deep iceberg furrows in the JOIDES Trough that record the initial episode of ice-shelf collapse. (*C*) Back-stepping marginal landforms (grounding zone wedges and moraines) imply continuous retreat of the grounding line southward in the JOIDES Trough and westward onto the slope of Crary Bank. Multibeam data shown in *B* and *C* were acquired on cruise NBP15-02 using a Kongsberg EM122 in dual-swath mode with 1° × 1° array and 12-kHz frequency. Base map modified from GeoMapApp. Central Basin (CB), Crary Bank (CrB), Eastern Basin (EB), eastern Ross Sea (ERS), Glomar-Challenger Basin (GC), JOIDES Trough (JT), Mawson Bank (MB), McMurdo Sound (McM), North Drygalski Trough (NDT), Pennell Bank (PB), Pennell Trough (PT), Ross Bank (RB), Ross Ice Shelf (RIS), South Drygalski Trough (SDT), Victoria Land Basin (VLB), Western Ross Sea (WRS).

collapse and onset of open marine conditions at this location as having occurred after 18 ka.

Along the eastern flank of Crary Bank, grounding line marginal features curve around and migrate up the flanks of the bank (Fig. 1*C*). The marginal features terminate at the bank margin where a prominent grounding zone wedge exists. Linear furrows occur seaward of this bank-margin wedge and indicate that calving was occurring at a water depth of ∼250 m. These observations corroborate previous results indicating that an ice shelf was grounded on banks in the western Ross Sea and shed sediments into adjacent troughs (14, 23).

Sediment cores from across the Ross Sea sampled a general stratigraphic succession of till and grounding line proximal deposits overlain by subice shelf sediments and capped by diatomaceous open marine sediments (14–17). Till and grounding line proximal deposits are poorly sorted mixtures of mud, sand and gravel with little or no biogenic material or organic carbon. They display little stratigraphic variability in texture and composition within individual cores.

Till and proximal glacial marine sediments are overlain by a thin (0–30 cm) mud unit with subtle grain size sorting, isolated occurrences of foraminifera, no diatoms, and only minor concentrations of ice-rafted material. We interpret this as a subice shelf deposit (16, 24). Resting above, and typically in sharp contact with, subice shelf sediments are diatomaceous sediments that contain variable concentrations of ice-rafted material, higher organic carbon, diatoms, and foraminifera. The contact between subice shelf and diatomaceous sediments marks the retreat of the ice shelf and the onset of open marine conditions. Analysis of cores collected during NBP cruises revealed that diatomaceous sediments extend across Ross Sea but are thickest on the outer, western continental shelf (Fig. 1*A*). This thickness trend is consistent with geomorphic evidence for an early phase of ice shelf retreat on the outer, western continental shelf.

Unfortunately, Ross Sea sediments are notoriously lacking in carbonate material needed for radiocarbon dating and AIO (acid insoluble organic) bulk radiocarbon dating is seriously biased by old (radiocarbon dead) carbon that is ubiquitous in Ross Sea sediments (14–18). As a result, prior attempts to constrain the timing of ice-shelf retreat and onset of open marine conditions have met with limited success.

Using select cores from the Ross Sea (Table S1), we measured ^{10}Be concentrations to further document ice-shelf breakup and compound-specific (CS) radiocarbon ages to constrain the timing of ice-shelf collapse (*Materials and Methods*, *SI Materials and Methods*, and Tables S2 and S3). Eastern Ross Sea cores show an abrupt down-core change in ^{10}Be concentrations, which is associated with a sharp contact between diatomaceous and terrigenous glacimarine sediments (Fig. 2 and Fig. S1). Core KC11, the most offshore site, displays a dramatic increase in ^{10}Be concentration ($0.33 \pm 0.15 \times 10^9$ to $3.40 \pm 0.30 \times 10^9$ atoms ^{10}Be per g) at 18-cm depth in the core, which is accompanied by a rapid increase in the abundance of diatom frustrales (Fig. 2*A* and Fig. S2). This change occurred at ∼5 ka, based on our CS radiocarbon chronology (Table S3), and is interpreted to indicate the timing of ice-shelf retreat landward of the core site. A similar but more gradual transition is observed in core TC07, recovered from the midshelf. At this site, ^{10}Be concentrations started to increase at about 4 ka (Fig. 2*B* and Fig. S2). The low concentration of ^{10}Be found in the lower sections of these cores implies (*i*) the last exposure of these sediments occurred before the Quaternary and inherited ^{10}Be has nearly completely decayed and (*ii*) there was little ^{10}Be advection under the ice shelf from the open ocean. Because inherited ^{10}Be is transported by glacial processes to the subice shelf environment, we argue that these sediments also contain abundant "old carbon" (i.e., >50,000 y old) similar to tills.

Core TC04 was recovered closest to the modern ice-shelf margin (Fig. 1*A*) and contains in excess of 0.25×10^9 atoms ^{10}Be per g in the shallower section (<9-cm depth in core), whereas low, constant ^{10}Be concentrations occur below that depth and indicate subice conditions (Fig. 2*C*). Although only one CS radiocarbon date is available for this core, the results indicate that the Ross Ice Shelf had retreated south of this location by 1.5 ka.

In the western Ross Sea, ^{10}Be concentrations and CS ages acquired from three cores (TC17, TC31, and GC1604; Fig. 3 and Fig. S3) are used to constrain the onset of open marine conditions. Core TC31 sampled the upper part of the transitional contact between subice shelf and diatomaceous sediments, based on correlation with associated piston core PC31. CS radiocarbon ages indicate that the calving line of the ice shelf retreated across this site at ∼5ka (Fig. 3).

Core TC17 sampled only open marine deposits, but based on correlation with associated piston core PC17 it bottomed-out just above the contact between diatomaceous sediments and subice

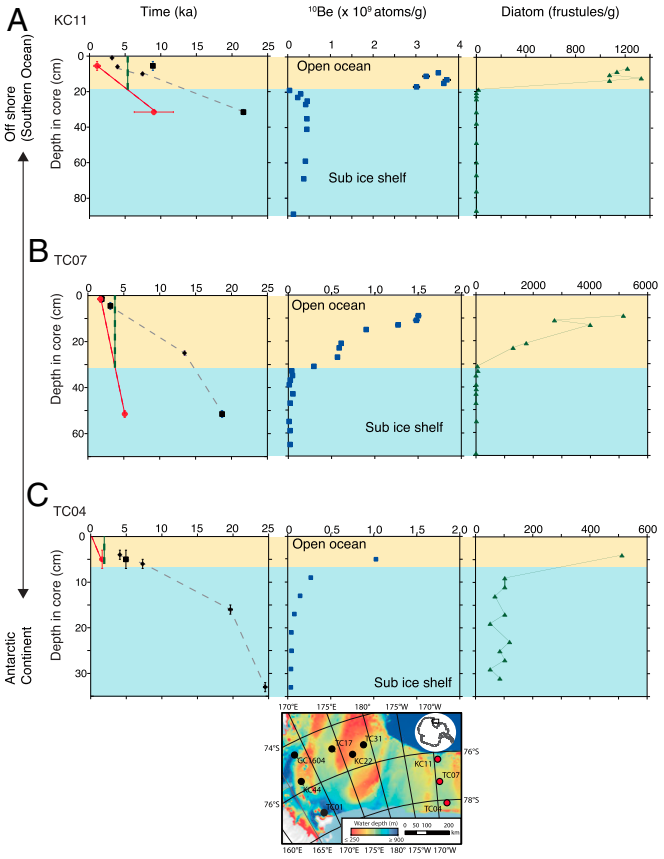

Fig. 2. Profiles of radiocarbon dates, ^{10}Be concentrations, and diatom concentrations in cores from the eastern Ross Sea (*A*–*C*). Radiocarbon dates of TOC obtained from previous studies (♦: ref. 16) and the present work (■) are plotted along with newly obtained radiocarbon dates of C14–C18 fatty acids (red circle; see *Supporting Information*). Green dotted lines in each panel indicate estimated timings of ice-shelf calving front crossing over the corresponding core sites based on ^{10}Be concentrations. Diatom abundance correlates well with ^{10}Be concentrations. Yellow indicates open-ocean conditions after ice-shelf retreat, whereas blue indicates subice-shelf conditions.

shelf sediments. It therefore provides a minimum age constraint for ice-shelf collapse at ∼5 ka (Table S3), consistent with late Holocene AIO ages from this core (Fig. 3*B*).

Core GC1604 records onset of open marine conditions in the westernmost Ross Sea (Fig. 1*A*). It sampled the ice-shelf retreat surface, which is manifest as an abrupt increase in ^{10}Be at 155 cm. CS radiocarbon ages for this core indicate onset of open marine conditions at ∼8 ka (Fig. 3*C*). The earlier timing of ice-shelf collapse suggests that an embayment existed in the ice front along the North Victoria Land coast. This is consistent with radiocarbon dates from shell, seal skin, and penguin remains from nearby Terra Nova Bay that indicate ice-free conditions by ∼8.2 cal ka B.P. (25) and the initiation of beach formation at ∼7 ka due to sufficient coastal wave energy resulting from reduced sea-ice cover (26).

CS age determinations on bank cores were not possible due to limited material available for dating. AIO ages of diatomaceous sediments from Pennell Bank (KC22) and Crary Bank (KC44) in the western Ross Sea (Fig. 1*A*) are both ∼6.5 cal ka B.P. (uncorrected for surface age). Using commonly reported surface corrections for AIO ages (∼2–4.5 ky; e.g., ref. 16), suggests that open marine conditions on the banks were established in the late Holocene, which is consistent with our CS ages from the other cores, with the exception of core GC1604.

The stages of grounding line and ice-shelf retreat in the western Ross Sea are illustrated in Fig. 4.

Controls on Ice-Shelf Collapse. To date, work has yielded no direct evidence of why the ice shelf retreated from the Ross Sea continental shelf. We use a recently developed 3D thermodynamic ice-shelf model (27) that addresses oceanographic influence on ice-shelf instability. Temperature records from ice cores are used to assess the influence of atmospheric warming on ice-shelf retreat in the mid-to-late Holocene.

The numerical model calculates 3D ocean circulation and the ice shelf–ocean thermal interaction under a fixed ice-shelf configuration and is used to estimate basal melt rates of the Ross Ice Shelf with a 15-km horizontal grid spacing. When run under the present-day configuration (ocean bathymetry, ice front line, grounding line, and ice shelf draft and climatological atmospheric condition), this model reasonably reproduces modern melt rates for all of the ice shelves fringing the Antarctic continent. Past melt rates are calculated at four stages of ice-shelf retreat, listed using the ice front (i.e., calving line) and grounding lines indicated therein (Fig. 5). Ice-shelf thickness is assumed to be 200 m and 450 m within 50 km and outside of 500 km, respectively, from the ice front and changes linearly in between. Atmospheric conditions for these runs are the same as in the present-day run. We perform a 30-y simulation for each experiment. After ∼15 y, modeled basal melting of the ice shelf reaches a quasi-steady state, and thus we use the model results averaged over the last 5 y.

There are primarily three types of water in the Ross Sea including shelf water (SW), CDW, and Antarctic surface water (AASW). SW is produced during the winter due to brine rejection in near-freezing or freezing surface water. CDW is converted to modified CDW (MCDW) as it flows southward toward the ice shelf and mixes with colder ambient waters on the continental shelf. Sea ice melt produces AASW, which is a low-salinity water mass. Among these water masses, CDW and MCDW have the highest

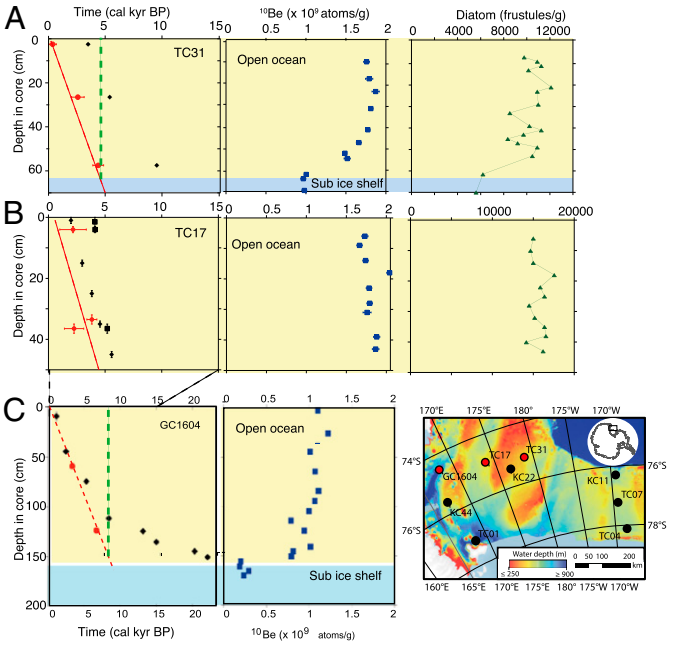

Fig. 3. Radiocarbon dates, ^{10}Be concentrations, and diatom concentrations in cores TC17, TC31, and GC1604 (*A*–*C*) from the western Ross Sea (red filled circles in inset map show core locations). Correlation of cores TC 17 and TC31 and their associated piston cores PC 17 and PC31 was done using lithological information and AIO ages from both cores to establish that the base of core TC31 sampled the transition between subice shelf and open marine sediments, consistent with the decrease in ^{10}Be in the bottom of the core, and core TC 17 bottomed out just above this transition.

temperature and the greatest potential for causing basal melting of the ice shelf (28).

The ratios of temperature and total volume transport of inflowing water masses for each experiment are shown in Fig. S4. More warm water reaches the subice shelf cavity when the grounding line is located in a more seaward location. The results of our modeling effort suggest that the melting rate at the bottom of the Ross Ice Shelf was *ca*. 180 Gt·y^{-1}, equivalent to *ca*. 1.5 times larger than present basal melt estimated in the control run (i.e., present case: Fig. S4). The most pronounced ice-shelf melting occurs in the western Ross Sea due to warmer CDW, a consequence of shorter residence time of MCDW on the continental shelf. In fact, analysis aimed at estimating subice shelf water temperatures during the Holocene indicate much warmer water beneath the ice shelf at 5 ka compared with the present Fig. S4 (*SI Materials and Methods*), consistent with widespread ice-shelf collapse across the Ross Sea.

Ice core δ^{18}O records from the EAIS suggest that Holocene warming occurred around 8 ka (29). In contrast, the Byrd δ^{18}O record from West Antarctica shows a rapid increase in atmospheric temperatures of about 2 °C at around 4.5 ka. This perhaps reflects differences in local ice thickness or changes in the moisture source (30, 31). However, the Siple Dome ice core contains abundant melt layers that began to increase in frequency around 7 ka and became more prominent by 4 ka, suggesting elevated summer air temperature during the late Holocene (32). The timing of final collapse of the ancestral Ross Ice Shelf is consistent with rapid thinning of an EAIS outlet glacier initiating at ∼7 ka followed by gradual thinning well into the late Holocene (33). Additionally, these observations are consistent with glaciological observations at Roosevelt Island that indicate division of flow around the island followed by thinning of ∼9 cm·y^{-1} since ∼4–3 ka (34, 35). Thus, ice-shelf retreat in the Ross Sea is consistent with ice-core records of atmospheric warming in the region. Timing of ice-shelf retreat observed here is also well correlated with far-field Holocene sea level records (36–38). Further CS radiocarbon age constraints of grounding-line retreat and ice-shelf collapse around Antarctica will help identify the relationship and phasing of regional and global climate, oceanographic, and sea-level variations in the late Pleistocene and Holocene.

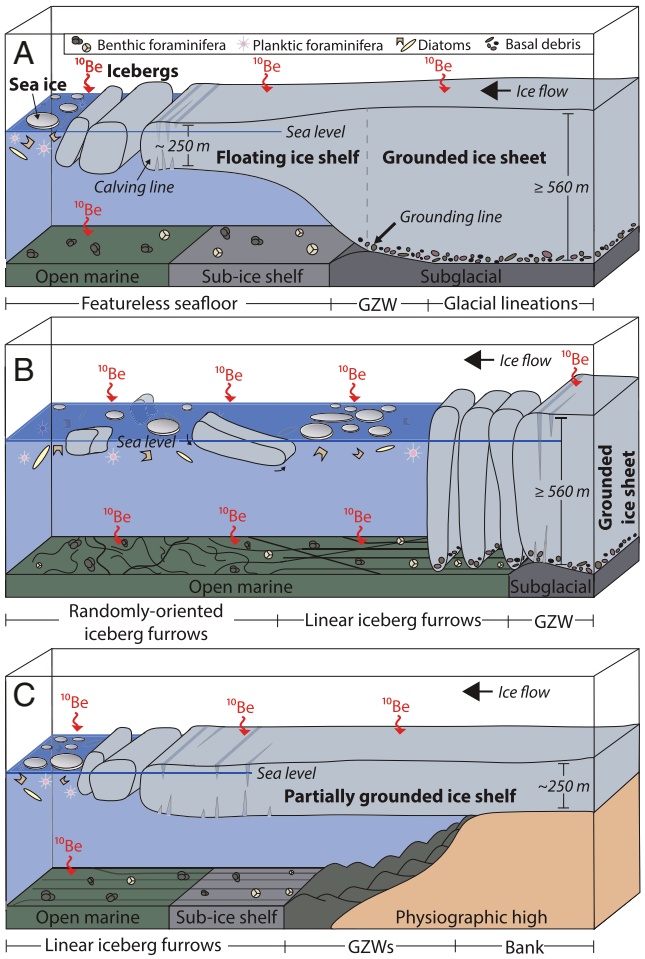

Fig. 4. Schematic illustration of events described in the text. (*A*) During the LGM the ice sheet and associated ice shelf extends across the outer continental shelf. A grounding zone wedge marks the LGM grounding line position. Subice shelf deposits contain rare foraminifera but lack diatoms and ^{10}Be. Diatoms and ^{10}Be in sediments indicate seasonally open marine conditions. (*B*) An initial episode of ice-shelf collapse and associated grounding line retreat on the outer, western continental shelf occurred shortly after the LGM. Ice-shelf breakup resulted in clusters of deep-keeled icebergs that cut linear furrows at the depth of the former grounding line (−560 m). As icebergs began to disperse they formed randomly oriented furrows. (*C*) Continuous retreat of the grounding line in the western Ross Sea is marked by marginal landforms that back-step continuously within troughs and onto banks. An ice shelf is grounded on banks and extends across the middle and inner continental shelves of the western and eastern Ross Sea until the late Holocene, when final breakup occurs. Illustration not to scale.

Conclusions

The geologic record provides compelling evidence of widespread and rapid ice-shelf retreat in the Ross Sea. An early episode of ice-shelf collapse was confined to the outer continental shelf of the western Ross Sea and was followed by an episode of continuous grounding-line retreat. This was followed by an extended period when an ice shelf covered the entire eastern continental shelf and most of the western shelf. Newly acquired ^{10}Be measurements and diatom abundances from select cores provide supporting evidence for ice-shelf retreat and CS radiocarbon ages constrain the onset of the most widespread retreat as occurring at ∼5 ka. Modeling results coupled with ice-core temperature records indicate that ice-shelf collapse was caused by combined atmospheric warming and warm ocean currents impinging on the continental shelf. Initial ice-shelf retreat in the western Ross Sea was slowed by the stabilizing effect of shallow banks; however, the modern ice shelf has fewer pinning points than its late Holocene predecessor, making it more vulnerable to climate and oceanographic influences. The sensitivity of the Ross Ice Shelf in the late Holocene to atmospheric and oceanic warming suggests modern accelerated warming may lead to instabilities in the modern ice shelf.

Materials and Methods

Carbonate material in Ross Sea sediments is sparse and AIO fraction ages have proven unsuitable for constraining ice-shelf retreat and the onset of open-marine conditions. Ross Sea sediments are known to contain enough old carbon (radiocarbon dead) to seriously bias AIO ages, especially terrigneous glacimarine sediments (14–18, 34). To more accurately determine the marine components of glacimarine sediments and better constrain ice-shelf retreat, we used CS radiocarbon dating of C14, C16, and C18 fatty acids isolated from the bulk sediment in six cores, three from the eastern Ross Sea and three from the western Ross Sea (Fig. 1*A* and Table S1). Although these compounds are derived from various organisms, they contain very little relict organic matter due to rapid decomposition (39). Thus, CS radiocarbon dating can provide accurate ages that are unaffected by reworked organic material from interior Antarctica.

We further measured the concentration of cosmogenic ^{10}Be (half-life of 1.387 My) in the sediments to identify the timing of ice-shelf edge retreat across the core locations. Following ice-shelf retreat, atmospherically produced ^{10}Be, which quickly attaches to ambient aerosols, immediately begins to accumulate at the seafloor. This proxy was first applied to sediment taken from underneath the WAIS and revealed that the Ross Embayment previously experienced open-marine conditions (40). Subsequent systematic analysis reveals a significant difference in seafloor ^{10}Be concentrations, depending on whether the site was covered by a permanent floating ice canopy (41). Thus, down-core ^{10}Be variations are a proxy for reconstructing ice-shelf retreat

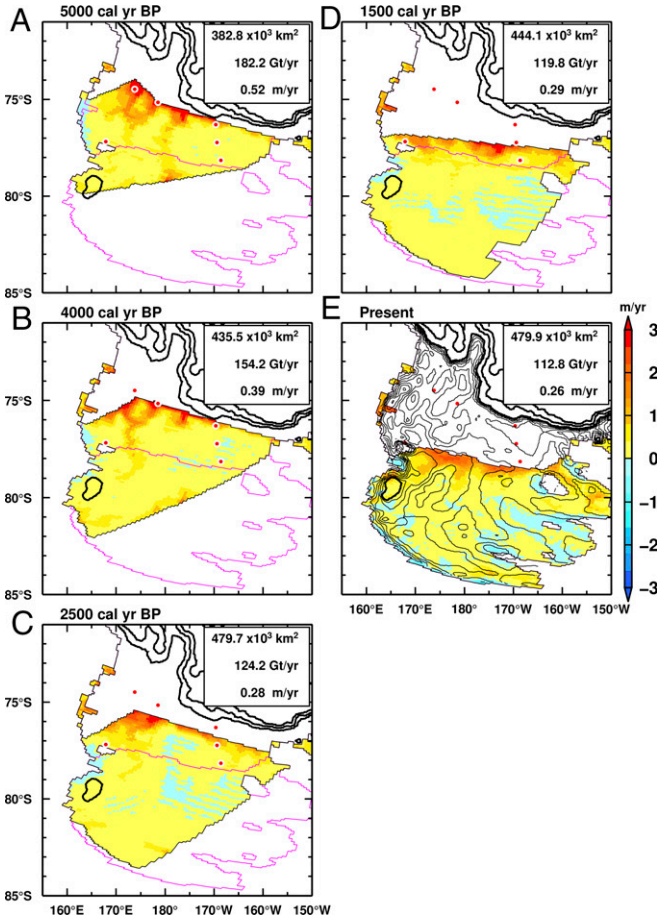

Fig. 5. (*A*–*E*) Spatial distribution of basal melting/freezing rate (meters per year) of ice shelves in different geometric configurations based on the model results (27). Core locations of the present study are shown as red dots and positive values indicate melting of ice for each time interval. Thick and thin black contours indicate bottom depths with 1,000-m and 100-m intervals, respectively. Red lines in the figure indicate the present ice front and grounding line locations. Areal extent, quantities of basal melting, and mean melting rate are listed in the inset in each panel.

history, and this has not been previously applied to Antarctic marine sediments. Complementary to the ^{10}Be measurements as a proxy for ice-margin retreat, diatom abundance was also determined (Fig. S1).

Radiocarbon Dating on Sedimentary Fatty Acids. Dried sediment was extracted with dichloromethane/methanol (CH_2Cl_2/MeOH, 7:3, vol/vol), and the total extract was saponified with 0.5 M KOH/MeOH under reflux. Neutral components were removed from the saponified material by extraction with *n*-hexane. Then, the acidic fraction was extracted with CH_2Cl_2 after the remaining solution was acidified to <pH 2 with hydrochloric acid (HCl). The acidic fraction was esterified with HCl/MeOH. Silica gel column chromatography of the methylated acidic fraction was used to separate the fatty acid methyl esters (FAMEs) with *n*-hexane/CH_2Cl_2 (2:1, vol/vol) from other polar compounds. Reversed-phase high performance liquid chromatography (HPLC) was used to isolate the saturated C14, C16, and C18 FAMEs from the rest of the FAME fraction. We used three columns (Develosil C30-UG-5, 4.6 × 250 mm, 5.5-μm particle size; Nomura Chemical) connected in series. The mobile phase was MeCN/MeOH (1:2, vol/vol) with 0.5% pyridine. The column oven temperature was 15 °C from 0 to 35 min, ramped at 2 °C·min^{-1} from 35 to 52.5 min and held at 50 °C until 80 min. The HPLC system comprised a binary pump (Agilent G1312A), on-line degasser (Agilent G1379B), auto sampler (Agilent G1313A), total temperature controller (Polaratherm Series 9000), evaporative light scattering detector (ELSD; Polymer Laboratories PL-ELS 2100), and fraction collector (Agilent G1364C). Data were collected and processed using Agilent Chemstation software. Conditions for the ELSD were as follows: nebulizer, 30 °C; evaporator, 35 °C; gas flow, air; 1.2 SLM (standard liters per minute; l min^{-1} at 25 °C, 414 kPa in the mass flow controller). The flow rate of the mobile phase was 1 mL·min^{-1}.

The isolated fraction was then subjected to the above described silica gel column chromatography conditions to remove impurities introduced during HPLC. The C14, C16, and C18 FAMEs can be eluted with *n*-hexane/CH2Cl2 (2:1, vol/vol). An aliquot of the silica gel elute (up to 1% of the total amount) was transferred to another vial, concentrated, and examined using GC/MS and NMR to evaluate the purity of the target FAMEs.

Typically 30–110 μg of C14–C18 FAMEs were collected and converted to graphite (Table S2). Target graphite samples were then measured at the W. M. Keck Carbon Cycle Accelerator Mass Spectrometry facility at the University of California, Irvine. Radiocarbon for total organic carbon was measured at the accelerator MS facility of the University of Tokyo (42). All radiocarbon values were corrected for the contribution of methyl carbon obtained from MeOH ($\Delta^{14}C = -991‰$) during the esterification by isotope mass balance. We have monitored the blank by various methods including gas chromatography, NMR, and elemental analyses. NMR spectroscopy using a 1-mm microliter NMR probe should be useful for detecting contaminants (10 μg or less), such as compounds whose molecular weight is greater than 600 Da. As demonstrated in Fig. S5, a proton NMR spectrum of C-16 FAME (61 μg) isolated from the sediment with the method described in the paper shows that all spectra can be assigned to either from C-16 FAME or NMR solvent and did not observe peaks originating from other compounds. Therefore, impurities should be lower than the detection limit of NMR spectroscopy (less than *ca*.1 μg).

Parallel blank experiments were conducted simultaneously with the samples using the same procedure, including solvent extraction, liquid/liquid extraction, silica gel column chromatography, and derivatization (i.e., methyl esterification). During these blank experiments, we observed two major fatty acids in the gas chromate/mass spectrometry analysis. They are C16 fatty acid (palmitic acid) and C18 fatty acid (steric acid). We quantified these peaks and found that the total amount of these fatty acids is *ca*. 0.2 μg C on average. This amount corresponds to only 0.2–0.7% of the actual sample size for radiocarbon dating (cf. 30–110 μg C). Assuming that the real sample age is 5,000 y B.P., and that above blank (i.e., contaminants) exhibits an extreme age, such as either modern or ^{14}C-dead, such a low blank level could shift age younger or older only less than 100 y. Thus, we conclude that chemical extraction step blank will not have a significant effect on the results presented here.

Graphite sample sizes are significantly correlated with the background, requiring correction of this effect. A correction was applied to each sample using the sample size–background relationship obtained from measurement of IAEA-C4 (wood: $\Delta^{14}C = -998.0$ to $-995.6‰$). Calibration of ^{14}C ages was performed with CALIB 7.0 and the Marine13 calibration curve (43) with a total reservoir age of 1,300 ± 100 y (44, 45).

Coupled Ice Shelf–Sea Ice–Ocean Model Experiments. We use a sea-ice–ocean model ("COCO") (46) with an ice-shelf component. The coupled model is the same as in ref. 27, so only a brief outline of the model setup is presented here. The model domain is the Southern Ocean and the artificial northern boundary is placed at 35° S. We use an orthogonal, curvilinear, horizontal coordinate system. The singular points are placed on East Antarctica (82° S, 45° E) and the North Pole. The horizontal grid spacing over Antarctic coastal regions is between 10 and 20 km; thus, we represent almost all of the Antarctic ice shelves in a single model. The horizontal grid spacing around the Ross Ice Shelf is about 15 km. The present-day bathymetry and ice-shelf draft are calculated from the RTopo-1 dataset (47). Initial values for temperature and salinity fields are derived from Polar Science Center Hydrographic Climatology (48), and the ocean velocity is set to zero over the model domain. In the northern six grids, temperature and salinity are restored to the monthly climatology throughout the water column. Surface boundary conditions on the open ocean and sea ice are wind stresses, wind speed, air temperature, specific humidity, downward shortwave radiation, downward longwave radiation, and freshwater flux. These boundary conditions are calculated from the atmospheric surface dataset of ref. 49. With this configuration, the model can reproduce the distribution and amount of basal melt of the Antarctic ice shelves, in particular the Ross Ice Shelf, in the present-day configuration (27).

We performed four experiments for past ice-front configurations (5,000 y B.P., 4,000 y B.P., 2,500 y B.P., and 1,500 y B.P.; Fig. 5). Past ice-front locations are estimated from this study using cores obtained from the Ross Sea. In the past configurations, ice-shelf thickness is assumed to be 200 m and 450 m within 50 km and outside of 500 km, respectively, from the ice front and to change linearly in between. For simplicity of comparison, the atmospheric conditions for past configurations are assumed to be the same as the present-day conditions. We perform a 30-y simulation for each experiment. After about 15 y of integration, modeled basal melting of the ice shelf reaches a quasi-steady state, and thus we use the model results averaged over the last 5 y.

ACKNOWLEDGMENTS. We thank C. Sawada, M. Toyoda, M. Iwai, and H. Matsuzaki for laboratory assistance and S. Obrochta for discussion. This work was supported by National Science Foundation Polar Programs Grant ANT-0837925 (to J.B.A.), Japan Society for the Promotion of Science (JSPS) NEXT program Grant GR031, JSPS Grant KAKENHI-26247085 (to Y.Y.), and Rice University (Wiess Visiting Professorship, to Y.Y.).

1. Scambos TA, Hulbe C, Fahnestock M, Bohlander J (2000) The link between climate warming and break-up of ice shelves in the Antarctic Peninsula. *J Glaciol* 46:516–530.
2. Skvarca P, De Angelis H (2003) *Antarctic Peninsula Climate Variability: Historical and Paleoenvironmental Perspectives*, eds Domack E, Leventer A, Burnett A, Bindschadler RA, Convey P, Kirby M (American Geophysical Union, Washington, DC), Vol 79, pp 69–78.
3. Scambos TA, Bohlander JA, Shuman CA, Skvarca P (2004) Glacier thinning after ice shelf collapse in the Larsen B embayment, Antarctica. *Geophys Res Lett* 31:LI18402.
4. Jenkins A, et al. (2010) Observations beneath Pine Island Glacier in West Antarctica and implications for its retreat. *Nat Geosci* 3:468–472.
5. Jacobs SS, Jenkins A, Giulivi CF, Dutrieux P (2011) Stronger ocean circulation and increased melting under Pine Island Glacier ice shelf. *Nat Geosci* 4:519–523.
6. Bentley MJ, et al. (2005) Early Holocene retreat of the George VI Ice Shelf, Antarctic Peninsula. *Geology* 33:173–176.
7. Smith JA, et al. (2007) D.E. Oceanic and atmospheric forcing of early Holocene ice shelf retreat, George VI ice shelf, Antarctic Peninsula. *Quat Sci Rev* 26:500–516.
8. Jakobsson M, et al. (2011) Geological record of ice shelf break-up and grounding line retreat, Pine Island Bay, West Antarctica. *Geology* 39:691–694.
9. Kirshner AE, et al. (2012) Post-LGM deglaciation in Pine Island Bay, West Antarctica. *Quat Sci Rev* 38:11–26.
10. Dupont TK, Alley RB (2005) Assessment of the importance of ice-shelf buttressing to ice-sheet flow. *Geophys Res Lett* 32:L04503.
11. Schoof C (2007) Ice sheet grounding line dynamics: Steady states, stability, and hysteresis. *J Geophys Res* 112:1–19.
12. Anderson JB, Shipp SS, Lowe AL, Wellner JS, Mosola AB (2002) The Antarctic ice sheet during the last glacial maximum and its subsequent retreat history: A review. *Quat Sci Rev* 21:49–70.
13. Bentley MJ, et al. (2014) A community-based geological reconstruction of Antarctic Ice Sheet deglaciation since the Last Glacial Maximum. *Quat Sci Rev* 100:1–9.
14. Anderson JB, et al. (2014) Ross Sea paleo-ice sheet drainage and deglacial history during and since the LGM. *Quat Sci Rev* 100:31–54.
15. Cunningham WL, Leventer A, Andrews JT, Jennings AE, Licht KJ (1999) Late Pleistocene-Holocene marine conditions in the Ross Sea, Antarctica: Evidence from the diatom record. *Holocene* 9:129–139.
16. Domack E, Jacobson E, Shipp S, Anderson J (1999) Late Pleistocene-Holocene retreat of the West Antarctic Ice Sheet in the Ross Sea: Part 2 – Sedimentologic and stratigraphic signature. *Geol Soc Am Bull* 111:1517–1536.
17. Mosola AB, Anderson JB (2006) Expansion and rapid retreat of the West Antarctic Ice Sheet in Eastern Ross Sea: Possible consequence of over-extended ice streams? *Quat Sci Rev* 25:2177–2196.
18. Licht KJ, Andrews JT (2002) The C-14 record of Late Pleistocene ice advance and retreat in the central Ross Sea, Antarctica. *Arc Ant and Alpine Res* 34:324–333.
19. Whitehouse PL, Bentley MJ, Le Brocq AM (2012) A deglacial model for Antarctica: Geological constraints and glaciological modeling as a basis for a new model of Antarctic glacial isostatic adjustment. *Quat Sci Rev* 32:1–24.
20. Deschamps P, et al. (2012) Ice-sheet collapse and sea-level rise at the Bølling warming 14,600 years ago. *Nature* 483(7391):559–564.
21. Yokoyama Y, Esat TM (2011) Global climate and sea level-Enduring variability and rapid fluctuations over the past 150,000 years. *Oceanography (Wash DC)* 24:54–69.
22. Stone JO, et al. (2003) Holocene deglaciation of Marie Byrd Land, West Antarctica. *Science* 299(5603):99–102.
23. Shipp S, Anderson JB, Domack EW (1999) Seismic Signature of the Late Pleistocene Fluctuation of the West Antarctic Ice Sheet System in Ross Sea: Part 1 - A New Perspective. *Geol Soc Am Bull* 111:1486–1516.
24. Anderson JB, Kennedy DS, Smith MJ, Domack EW (1991) Sedimentary facies associated with Antarctica's floating ice masses. *Paleoclimatic Interpretation of Glacial Marine Deposits*, eds Anderson J, Ashley G (Geological Soc. of America, Boulder, CO), Special Publication 261, pp 1–25.
25. Baroni C, Hall BL (2004) A new Holocene relative sea-level curve for Terra Nova Bay, Victoria Land, Antarctica. *J Quat Sci* 19:377–396.
26. Simkins LM, Simms AR, DeWitt R (2015) Assessing the link between coastal morphology, wave energy, and sea ice throughout the Holocene from Antarctic raised beaches. *J Quat Sci* 30:335–348.
27. Kusahara K, Hasumi H (2013) Modeling Antarctic ice shelf responses to future climate changes and impacts on the ocean. *J Geophys Res* 118:2454–2475.
28. Jacobs SS, Hellmer HH, Doake CSM, Jenkins A, Frolich RM (1992) Melting of ice shelves and the mass balance of Antarctica. *J Glaciol* 38:375–387.
29. Masson-Delmotte V, et al. (2011) A comparison of the present and last interglacial periods in six Antarctic ice cores. *Clim Past* 7:397–423.
30. Steig EJ, et al. (2000) Wisconsinan and Holocene climate history from an ice core at Taylor Dome, western Ross Embayment, Antarctica. *Geogr Ann, Ser A* 82:213–235.
31. Jouzel J, et al. (2001) A new 27 ky high resolution East Antarctic climate record. *Geophys Res Lett* 28:3199–3202.
32. Das SB, Alley RB (2008) Rise in frequency of surface melting at Siple Dome through the Holocene: Evidence for increasing marine influence on the climate of West Antarctica. *J Geophys Res* 113:D02112.
33. Jones RS, et al. (2015) Rapid Holocene thinning of an East Antarctic outlet glacier driven by marine ice sheet instability. *Nat Commun* 6:8910.
34. Conway H, Hall BL, Denton GH, Gades AM, Waddington ED (1999) Past and future grounding line retreat of the west Antarctic Ice Sheet. *Science* 286(5438):280–283.
35. Martin C, Hindmarsh RC, Navarro F (2006) Dating ice flow change near the flow divide at Roosevelt Island using a thermomechanical model to predict radar stratigraphy. *J Geophys Res* 111:F01011.
36. Lambeck K, Rouby H, Purcell A, Sun Y, Sambridge M (2014) Sea level and global ice volumes from the Last Glacial Maximum to the Holocene. *Proc Natl Acad Sci USA* 111(43):15296–15303.
37. Yokoyama Y, et al. (2012) Holocene sea-level change and Antarctic melting history derived from geological observations and geophysical modeling along the Shimokita Peninsula, northern Japan. *Geophys Res Lett* 39:L13502.
38. Yokoyama Y, Maeda Y, Okuno J, Miyairi Y, Kosuge T (2015) Holocene Antarctic melting and lithospheric uplift history of the southern Okinawa trough inferred from mid- to late-Holocene sea level in Iriomote Island, Ryukyu, Japan. *Quat Int*, 10.1016/j.quaint2015.03.030.
39. Ohkouchi N, Eglinton TI, Hays JM (2003) Radiocarbon dating of individual fatty acids as a tool for refining Antarctic margin sediment chronologies. *Radiocarbon* 47:401–412.
40. Scherer RP, et al. (1998) Pleistocene collapse of the west antarctic ice sheet. *Science* 281(5373):82–85.
41. Sjunneskog C, Scherer R, Aldahan A, Possnert G (2007) ^{10}Be in glacial marine sediment of Ross Sea, Antarctica, a potential tracer of depositional environments and sediment chronology. *Nucl Instrum Methods Phys Res B* 259:576–583.
42. Yokoyama Y, Koizumi M, Matsuzaki H, Miyairi Y, Ohkouchi N (2010) Developing ultra small-scale radiocarbon sample measurement at the University of Tokyo. *Radiocarbon* 52:310–318.
43. Reimer PJ, et al. (2013) IntCal13 and Marine13 radiocarbon age calibration curves 0–50,000 years cal BP. *Radiocarbon* 55:1869–1887.
44. Berkman PA, Forman SL (1996) Pre-bomb radiocarbon and the reservoir correction for calcareous marine species in the Southern Ocean. *Geophys Res Lett* 23:363–366.
45. Hall BL, Henderson GM, Baroni C, Kellogg TB (2010) Constant Holocene Southern-Ocean 14C reservoir ages and ice-shelf flow rates. *Earth Planet Sci Lett* 296:115–123.
46. Hasumi H (2006) CCSR Ocean Component Model (COCO) version 4.0, CCSR Rep 25 (Center for Climate System Research, University of Tokyo, Tokyo).
47. Timmerman R, et al. (2010) A consistent data set of Antarctic ice sheet topography, cavity geometry, and global bathymetry. *Ear Sys Sci Data* 2:261–273.
48. Steele M, Morley R, Ernold W (2001) PHC: A global ocean hydrography with a high-quality Arctic Ocean. *J Clim* 14:2079–2087.
49. Röske F (2006) A global heat and freshwater forcing dataset for ocean models. *Ocean Model* 11:235–297.